Nano Research
DOI 10.1007/s12274-014-0602-0
Research Article
ISSN 1998-0124
CN 11-5974/O4

Thermal conductivity determination of suspended mono- and bilayer WS_2 by Raman spectroscopy

Namphung Peimyoo[1], Jingzhi Shang[1], Weihuang Yang[1], Yanlong Wang[1], Chunxiao Cong[1], and Ting Yu[1,2,3] (✉)

[1] *Division of Physics and Applied Physics, School of Physical and Mathematical Sciences, Nanyang Technological University, 637371 Singapore, Singapore*
[2] *Department of Physics, Faculty of Science, National University of Singapore, 117542 Singapore, Singapore*
[3] *Graphene Research Center, Faculty of Science, National University of Singapore,117546 Singapore, Singapore*

Received: 13 August 2014
Revised: 29 September 2014
Accepted: 2 October 2014

KEYWORDS
thermal conductivity,
tungsten disulfide,
Raman,
temperature dependence,
excitation power

ABSTRACT

We report the thermal conductivities of monolayer (1L) and bilayer (2L) WS_2 grown by chemical vapor deposition (CVD), which are determined by use of temperature and excitation dependences of E^1_{2g} and A_{1g} Raman modes. The first-order temperature coefficients of E^1_{2g} and A_{1g} modes in both supported and suspended WS_2 layers were extracted. The frequency shift of the A_{1g} mode with temperature is larger than that of the E^1_{2g} mode for 1L-WS_2, which is attributed to stronger electron–phonon coupling for the A_{1g} mode than that for the E^1_{2g} mode. Moreover, by use of the shift of the phonon mode induced by laser heating, the thermal conductivities at room temperature were estimated to be 32 and 53 W/(m·K) for 1L- and 2L-WS_2, respectively. Our results provide fundamental information about the thermal properties of WS_2 layers, which is crucial for developing applications of atomically-thin WS_2 devices.

1 Introduction

Two dimensional (2D) transition metal dichalcogenides (TMDs) have recently gained much interest due to their superior properties [1–3]. Unlike graphene, TMDs such as MoS_2, $MoSe_2$, WSe_2 and WS_2 have intrinsic bandgaps. In particular, these TMDs exhibit a transformation from an indirect- to direct-bandgap when the thickness is reduced to a monolayer [4–7], opening up various opportunities for electronic and optoelectronic device applications. Monolayer MoS_2 (1L-MoS_2), which has been more intensively studied than other TMD monlayers, exhibits strong photoluminescence (PL), and its field-effect transistors present high mobility and large on–off ratios [8]. Another interesting 2D TMD of 1L-WS_2 has a direct bandgap with a theoretical value of ~2.1 eV [9], slightly larger than that of 1L-MoS_2, while its bulk has an indirect band of ~1.3 eV [1, 9]. Ultrathin WS_2 layers recently have been fabricated by several techniques such as mechanical exfoliation [7, 10], chemical exfoliation [11] and chemical vapor deposition (CVD) [12–14]. The synthesis of TMDs via

Address correspondence to yuting@ntu.edu.sg

CVD offers large single domain sizes and isolated samples, which make it more feasible for researchers to investigate the fundamental properties of the material. We have demonstrated optically that the intrinsic PL of 1L-WS_2 triangles synthesized by CVD, is much more intense than that of 1L-MoS_2 [15], comparable with the results for the exfoliated 1L-WS_2 from bulk crystals [7]. Electrically, the field-effect transistors based on thin layers of WS_2 extracted from single crystal and CVD-grown 1L-WS_2 are found to have attractive in-plane mobilities and effective conductance modulation [16, 17]. In view of its remarkable optical and electrical properties, atomically thin WS_2 is a promising material to be explored for various applications such as light-emitting diodes and optical sensors. In addition, because of the unique symmery and strong spin orbital coupling in 1L-WS_2, it is also regarded as a natural candidate for the valleytronic research [18–20].

Experimental studies of temperature and excitation dependences of the vibrational modes are very helpful to interpret anharmonicity between phonons and in electron–phonon interactions [21, 22]. These measurements can provide the fundamental parameters of the material properties such as temperature coefficient and thermal conductivity, which are important for device applications. For instance, a material with a high thermal conductivity can rapidly dissipate heat, which is very helpful for preventing the breakdown of devices. Conventionally, the thermal conductivity can be measured by several methods, e.g. thermal bridge technique [23]. Nowadays, Raman spectroscopy is another effective approach to evaluate the thermal conductivities of 2D materials such as graphene [24, 25] and MoS_2 layers [26], through the shifts of Raman modes induced by laser heating. Meanwhile, Raman spectroscopy can provide a wealth of *in situ* information about the number of layers [27, 28], doping concentration [29, 30] and strain effect [31] in graphene and TMDs. To date, experimental studies of the thermal conductivities of TMD materials for 1L, 2L and even few layers have been limited [26, 32]. Very recently, values for the thermal conductivities of 34 [26] and 52 W/(m·K) [32] have been obtained for 1L- and few-layer MoS_2, respectively. A temperature-dependent Raman study of supported 1L-WS_2 recently has been reported [33], although its thermal conductivity has not been reported. To our best knowledge, direct experimental investigation of the thermal conductivities of suspended 1L- and 2L-WS_2 has not been reported so far.

Here we present temperature and excitation-power-dependent studies of the vibrational modes for CVD-grown suspended 1L- and 2L-WS_2 using micro-Raman spectroscopy, which allow us to determine their thermal conductivites. The excitation dependence has been measured by laser heating of the suspended sample and monitoring the frequency shift of the phonon mode. By analysing the changes of Raman modes in both temperature- and power-dependent measurements, the thermal conductivities of suspended 1L- and 2L-WS_2 have been evaluated. Our results provide basic information about the heat conduction in atomically thin WS_2 layers, which is very necessary for thermal manangement in various nanoelectronic applications.

2 Results and discussion

Figure 1(a) presents an optical image of a WS_2 island grown on the SiO_2/Si substrate by CVD. The individual triangle includes 1L at the outer and 2L at the centre of the island. The topological atomic force microscope (AFM) image is presented in Fig. 1(b), showing the smooth and clean surface of the as-grown sample. According to the AFM height profile, 1L-WS_2 typically has a thickness varying between 0.7 to 1 nm and ~1.4 nm for 2L, which is consistent with the S–W–S length. Figure 1(c) shows the fluorescence image of the same island in which the 1L region displays stronger emission than that of mechanically exfoliated 1L-MoS_2 recorded under identical conditions (Fig. S1 in the Electronic Supplementary Material (ESM)).

In PL measurements, the samples were excited by a 532 nm laser, if not otherwise specified. It is known that bulk WS_2 is an indirect bandgap semiconductor with a ~1.3 eV bandgap [1, 34], whereas 1L-WS_2 has a direct bandgap of 2.1 eV [1, 9]. In Fig. 1(e), one sharp PL peak centered at 1.96–1.98 eV is observed for 1L-WS_2, and the peak intensity becomes very weak with a slight red-shift for 2L-WS_2. The PL intensity in the measured spectral range nearly vanishes for the bulk

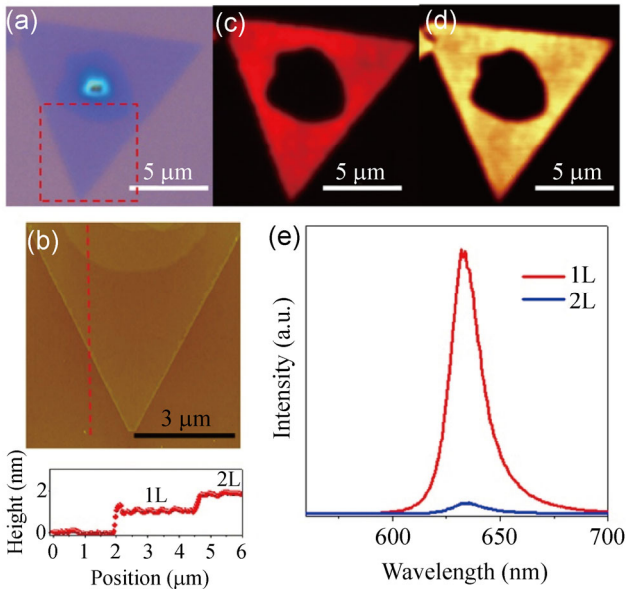

Figure 1 (a) Optical micrograph of a CVD-grown 1L-WS_2 triangular island with a second layer grown at the center of the island on SiO_2/Si substrate. (b) AFM image of the region highlighted in (a) and line scan along dashed line. Fluorescence image (c) and photoluminescence intensity mapping (d) exhibiting intense and spatially homogeneous contrast throughout the 1L region. (e) Photoluminescence spectra from 1L- and 2L-WS_2.

WS_2. When the thickness decreases to 1L, the dramatic increase of the PL intensity is a signature of the transformation from indirect to direct bandgap structures. In Fig. 1(d), the corresponding mapping of the PL intensity shows a spatial homogeneity over the 1L region. Uniform and intense emission indicates that these CVD samples have high crystalline quality [15].

Figure 2(a) shows the Raman spectrum of 1L-WS_2 at λ_{ex} = 532 nm. Most of the Raman modes for bulk and 1L-WS_2 [35–37] have previously been assigned. Raman active modes of bulk WS_2 comprise of A_{1g}, E_{1g}, E^1_{2g}, and E^2_{2g} at the centre of the Brillouin zone [35, 36], but E_{1g} is forbidden in our back-scattering configuration and the E^2_{2g} mode is less studied due to its low frequency out of most conventional Raman spectral ranges. Note that, according to lattice symmetry analysis [38], the precise notation of Raman modes in 1L-, 2L- and bulk WS_2 should be different. For simplification, the same notation of $A_{1g}(\Gamma)$ and $E^1_{2g}(\Gamma)$ was used for 1L-, 2L- and bulk WS_2 here. In 1L-WS_2, both $A_{1g}(\Gamma)$ and $E^1_{2g}(\Gamma)$ appear as an out-of-plane vibrational mode of sulphur atoms and an in-plane vibrational mode, respectively. The corresponding atomic vibration models are shown in the inset of Fig. 2(b). At λ_{ex} = 532 nm, the $A_{1g}(\Gamma)$ mode was observed at 417 cm^{-1} and a dominant 2LA(M) mode observed at ~350 cm^{-1} overlapping with the $E^1_{2g}(\Gamma)$ mode (355 cm^{-1}), which was acquired by multi-Lorentzian fitting, in agreement with other reports [35, 37]. Particularly, the perfect matching of the fitted curve to our experimental data was achieved when another additional peak (marked by the star (*)) at ~345 cm^{-1} was added. This peak is assigned to the $E^1_{2g}(M)$ mode according to theoretical phonon dispersion curves [39]. Moreover, Raman peaks at 296 and 320 cm^{-1} are the combination modes, which are attributed to 2LA(M) – 2 $E^2_{2g}(\Gamma)$ and 2LA(M) – $E^2_{2g}(\Gamma)$ modes, respectively. The Raman intensity of the 2LA(M) mode is much stronger than that of the $E^1_{2g}(\Gamma)$ mode at λ_{ex} = 532 nm, owing to the double resonance process [37]. At λ_{ex} = 488 nm (Fig. 2(b)), the intensity of the 2LA(M) mode is weaker than that of the $E^1_{2g}(\Gamma)$ mode. It is clearly shown that several peaks including second-order and combination modes become more apparent at λ_{ex} = 532 nm than those obtained at λ_{ex} = 488 nm. In detail, the Raman peaks at λ_{ex} = 532 nm in the ranges of 100–280 cm^{-1} and 560–730 cm^{-1} were enlarged as shown in the two insets of Fig. 2.

Figure 2(c) shows Raman spectra of 1L- and 2L-WS_2 at λ_{ex} = 532 nm. On the one hand, the $A_{1g}(\Gamma)$ mode blue-shifts with the increasing number of layers, similar to what is observed for MoS_2 layers [40], as van der Waals interactions between the layers increase the restoring force in thicker layers. On the other hand, the $E^1_{2g}(\Gamma)$ mode red-shifts with the increasing number of layers, which has also been observed in previous work. The decrease of phonon frequency has been attributed to increment of the dielectric long-range Coulomb interactions among the effective charges [39]. Raman intensity and frequency mappings of the $A_{1g}(\Gamma)$ mode for a triangular island are shown in Figs. 2(d) and 2(e), respectively. When the thickness increases, the integrated intensity of the mode increases and the peak blue-shifts, corresponding to the lighter colour region. As seen above, Raman spectra and mapping can be used as a fast approach to identify the thickness of thin layer WS_2.

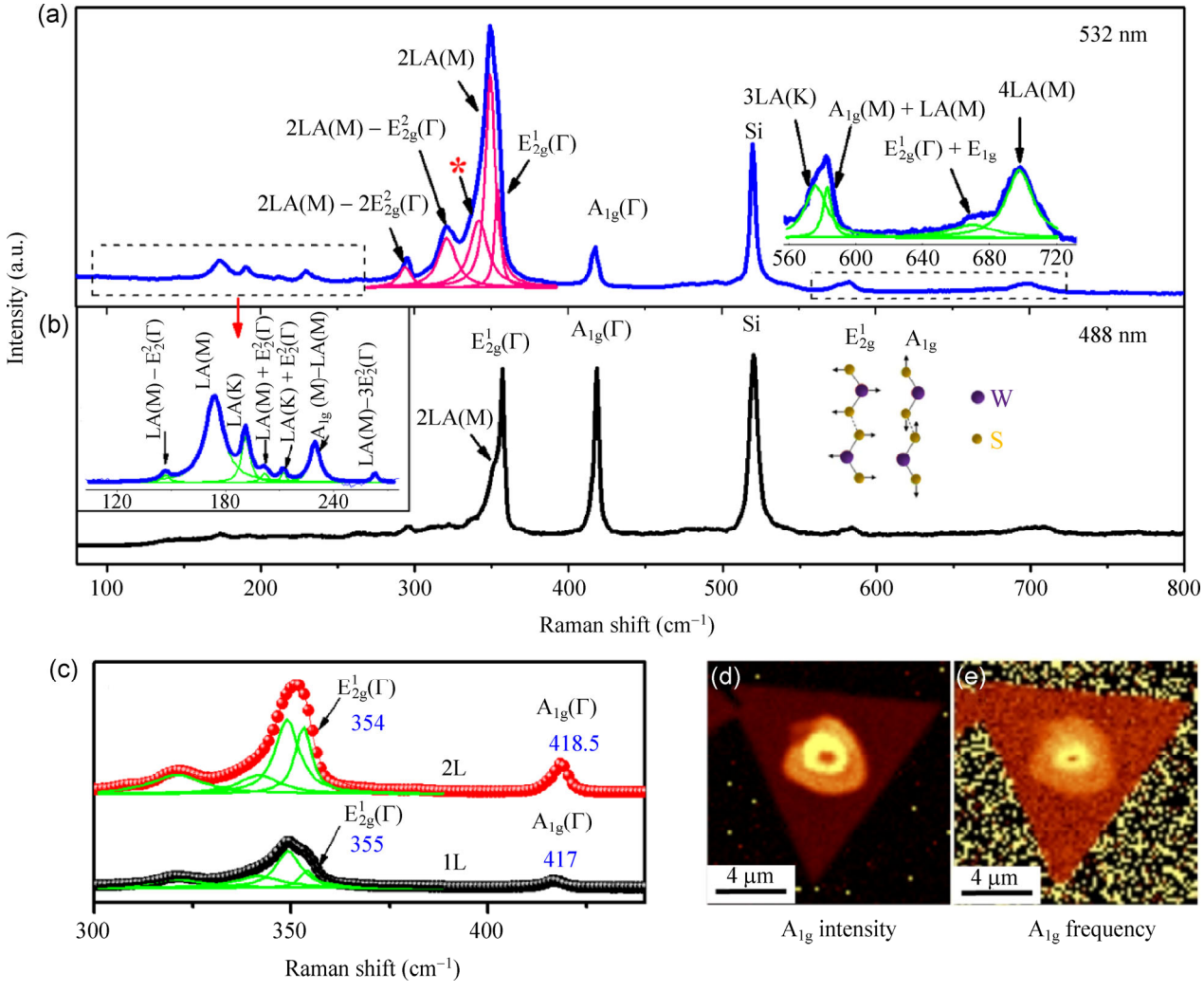

Figure 2 Raman spectra of 1L-WS_2 under different excitation wavelengths: 532 (a) and 488 nm (b). (c) Raman spectra of 1L- and 2L-WS_2 under 532 nm excitation laser line, showing a blue-shift and red-shift of the $A_{1g}(\Gamma)$ and the $E^1_{2g}(\Gamma)$ peak, respectively with an increase of thickness. Raman mappings for integrated intensity (d) and frequency (e) of the $A_{1g}(\Gamma)$ peak, showing that the Raman peak intensity in the 2L region is relatively stronger and the peak is blue-shifted with respect to 1L.

Temperature-dependent Raman measurements of supported 1L- and 2L-WS_2 were carried out at 80–380 K under 532 nm laser excitation. Figure 3(a) presents normalized Raman spectra of supported 1L-WS_2 in the peak regions of $E^1_{2g}(\Gamma)$ (left panel) and $A_{1g}(\Gamma)$ (right panel) collected at various temperatures. These Raman modes were analysed by multiple-peak Lorentzian fitting. The dependence of $E^1_{2g}(\Gamma)$ and $A_{1g}(\Gamma)$ peak frequencies on the temperature is plotted in Fig. 3(b). As expected, both $E^1_{2g}(\Gamma)$ and $A_{1g}(\Gamma)$ modes significantly red-shift with increasing temperature, analogous to what is observed for MoS_2 layers [26, 32, 41], and the changes of the G peaks in 1L and 2L graphene [22]. The temperature dependence of both Raman modes are linearly fitted by the following equation

$$\omega(T) = \omega_0 + \chi T \quad (1)$$

where ω_0 is the frequency of the $E^1_{2g}(\Gamma)$ or $A_{1g}(\Gamma)$ mode at 0 K and χ is the first-order temperature coefficient. The slopes of the dependences extracted from the linear fitting define the χ value, which are -1.25×10^{-2} and -1.49×10^{-2} cm^{-1}/K for the $E^1_{2g}(\Gamma)$ and $A_{1g}(\Gamma)$ modes, respectively. In addition to the shifts of Raman peak frequency, Raman spectra before normalization (Fig. S2 in the ESM) show increasing

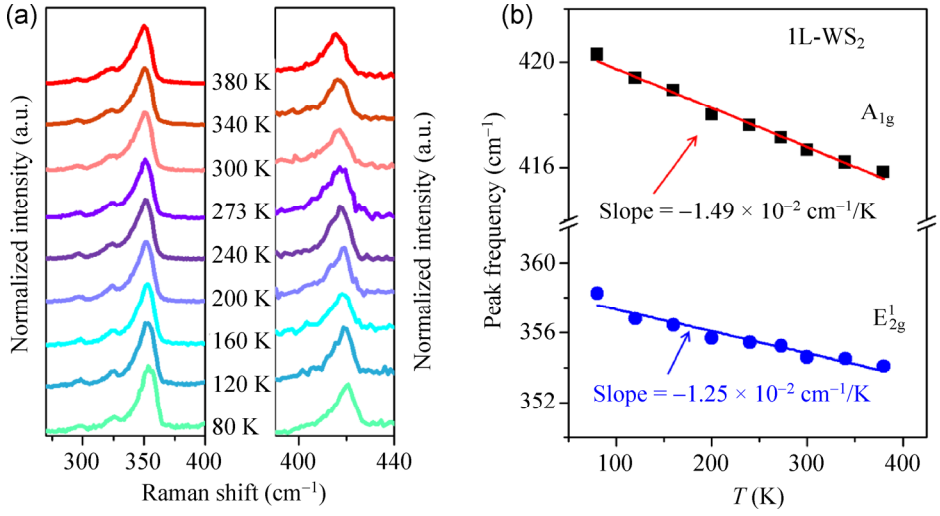

Figure 3 (a) Raman spectra of supported 1L-WS_2 showing Raman modes in the range of 240–400 cm^{-1} (left panel) and the $A_{1g}(\Gamma)$ mode (right panel) at various temperature in the 80–380 K range. (b) Frequencies of the $E^1_{2g}(\Gamma)$ and $A_{1g}(\Gamma)$ modes as a function of temperature. The linear fit to experimental data and slope values are shown.

Raman peak intensities when the temperature is raised, which is similar to that observed for 1L-MoS_2 and can be attributed to an increase in electron–phonon coupling [41].

Temperature effect measurements were also conducted on supported 2L-WS_2, and the typical red-shift behaviours of the $E^1_{2g}(\Gamma)$ and $A_{1g}(\Gamma)$ modes were observed (Fig. 4). For the 2L sample, the obtained temperature coefficient values of $E^1_{2g}(\Gamma)$ and $A_{1g}(\Gamma)$ modes are –1.33 × 10^{-2} and –1.21 × 10^{-2} cm^{-1}/K, respectively. According to previous studies [22, 32, 42, 43],

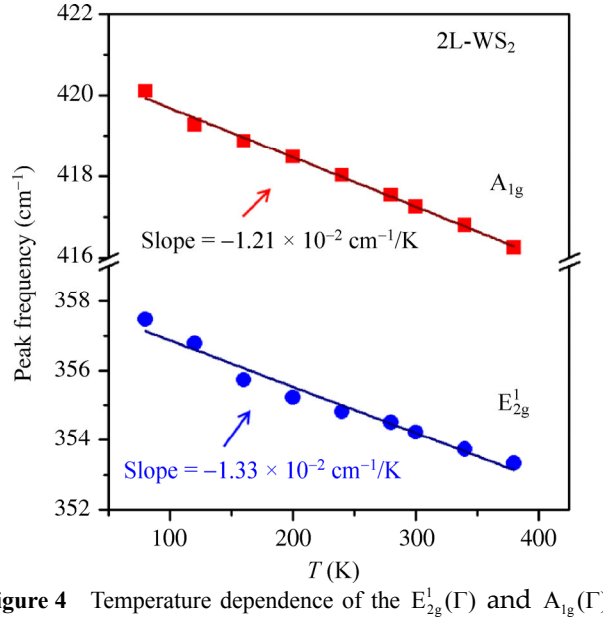

Figure 4 Temperature dependence of the $E^1_{2g}(\Gamma)$ and $A_{1g}(\Gamma)$ peak frequencies for supported 2L-WS_2.

the influence of temperature on these phonon modes includes two components: The intrinsic temperature contribution due to the anharmonicities of the phonon modes and the volume contribution caused by the thermal expansion of the crystal.

Moreover, in order to examine the potential substrate effect, similar temperature-dependent Raman measurements were performed for suspended 1L- and 2L-WS_2 samples. The as-grown WS_2 layers were transferred onto the substrates with holes of 3–6 μm in diameter as shown in Fig. 5(a). The laser beam size was approximately ~1 μm. Only 1L and 2L samples on the holes with the larger diameter of 6 μm were studied in order to minimize the undesired effects from the side wall of the hole, and to affirm that Raman signal is fully collected from the suspended layers rather than the supported region. In the temperature-dependent measurement for the suspended samples, it was found that both of the $E^1_{2g}(\Gamma)$ and $A_{1g}(\Gamma)$ modes show a linear red-shift with increasing temperature. The first-order temperature coefficients of the two modes for 1L and 2L are similar to those of the supported sample as shown in Figs. 5(c) and 5(d), respectively. This verifies that the substrate has a negligible effect on the temperature coefficients of Raman modes. The previous studies [26, 32] on suspended and supported MoS_2 layers are consistent with our observations here. Note that, the measurements have been conducted several times on different

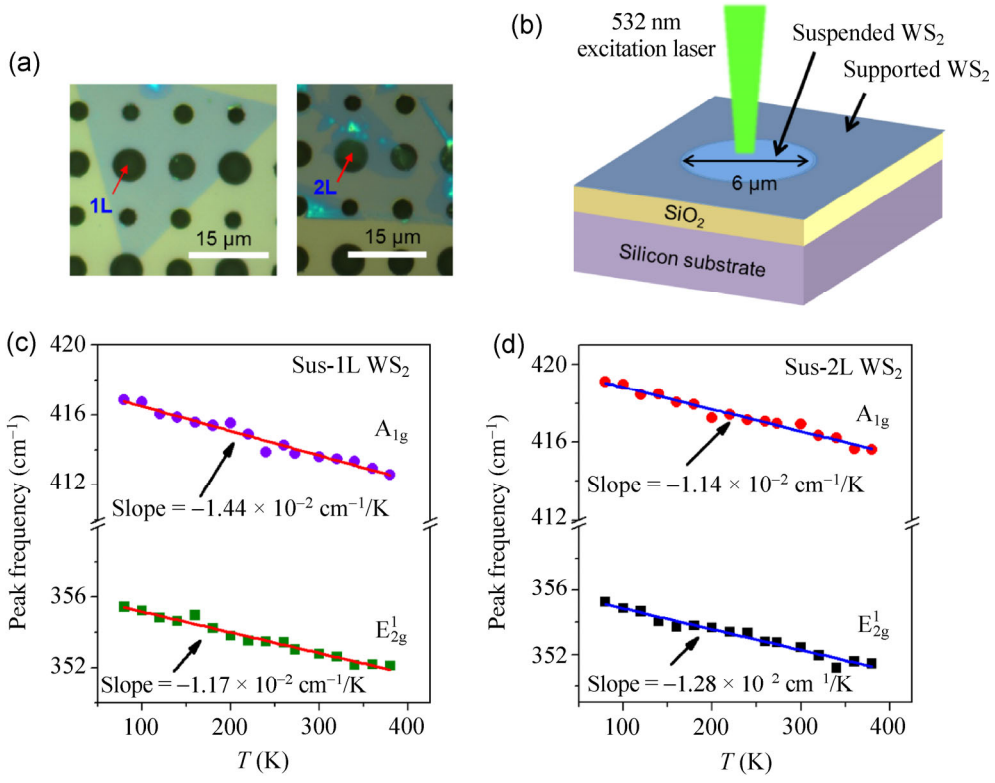

Figure 5 (a) Optical microscopy images of CVD-grown WS_2 layers transferred onto SiO_2/Si substrates chemically etched with an array of holes ~3–6 μm in diameter. The number of layers is labeled. (b) Schematic of the temperature-Raman measurements showing suspended WS_2 on SiO_2/Si substrates and the excitation laser light. Temperature dependence of $E^1_{2g}(\Gamma)$ and $A_{1g}(\Gamma)$ peak frequencies of suspended (c) 1L- and (d) 2L-WS_2, including linear fit and χ values.

supported and suspended samples to confirm the temperature dependence of the Raman modes and χ values. In comparison with the Raman peak frequencies of the supported samples, the peak frequencies of $E^1_{2g}(\Gamma)$ and $A_{1g}(\Gamma)$ modes from both suspended 1L and 2L samples shift by ~1–2 cm^{-1} (Fig. S3, in the ESM). For a 1L TMD, electrical doping causes a change of the A_{1g} peak frequency [29], whereas the frequency of the $E^1_{2g}(\Gamma)$ mode is found to be sensitive to strain [31, 44]. Thus, the small shifts of $E^1_{2g}(\Gamma)$ and $A_{1g}(\Gamma)$ frequencies between suspended and supported samples possibly arise from the slight differences of charge carrier concentration, and biaxial strain [44, 45] caused by the substrate effect, respectively. Further investigation is needed to clarify the effect of strain and doping.

It is worth noting that the linear dependence of the Raman peak frequencies with temperature has also been observed in graphene, MoS_2 layers and supported 1L-WS_2 [22, 26, 32, 33, 41]. A detailed summary of temperature coefficients (χ) of atomically thin TMDs and graphene is shown in Table 1. By comparison, $|\chi|$ values of the $E^1_{2g}(\Gamma)$ and $A_{1g}(\Gamma)$ modes in both supported- and suspended 1L- and 2L-WS_2 are of the same order as those for MoS_2 and graphene layers (for the G band). Note that, our $|\chi|$ values for Raman modes from 1L and 2L samples are approximately double those reported for supported 1L-WS_2 by another group [33]. In particular, in their results [33], the Raman frequencies of $E^1_{2g}(\Gamma)$ and $A_{1g}(\Gamma)$ modes barely change with temperature in the range ~80–250 K, whereas a linear dependence was observed throughout this temperature range in our samples. The discrepancy could be related to dielectric environment, temperature control, or the contact between sample and heat sink. Moreover, the response of Raman peak frequencies to temperature in 1L is different from that of 2L. The $|\chi|$ value of the $A_{1g}(\Gamma)$ mode for 1L-WS_2 is larger than that of the $E^1_{2g}(\Gamma)$ mode and vice versa for 2L-WS_2, similar to what was previously reported for 1L-MoS_2

Table 1 First-order temperature coefficients of the Raman modes from WS_2, MoS_2 and graphene layers

Sample	Comments	χ (cm^{-1}/K)		T (K)	λ_{ex} (nm)	Ref.
1L-WS_2	Supported, CVD	–0.0125	–0.0149	80–380	532	This work
1L-WS_2	Suspended, CVD	–0.0117	–0.0144	80–380	532	This work
2L-WS_2	Supported, CVD	–0.0133	–0.0121	80–380	532	This work
2L-WS_2	Suspended, CVD	–0.0128	–0.0114	80–380	532	This work
1L-WS_2	Supported, exfoliated	–0.0006	–0.0006	77–623	514.5	Thipuranthaka and Dattatray [33]
1L-MoS_2	Supported, CVD	–0.013	–0.016	~300–450	532	Lanzillo et al.[41]
Bulk MoS_2	Supported, CVD	–0.015	–0.013	~300–450	532	Lanzillo et al. [41]
1L-MoS_2	Suspended, exfoliated	–0.011	–0.013	100–320	514.5	Yan et al. [26]
1L-MoS_2	Supported, exfoliated	–0.017	–0.013	100–320	514.5	Yan et al. [26]
Few layer MoS_2	Supported, CVD	–0.0132	–0.0123	~83–523	532	Sahoo et al. [32]
1L graphene	Supported, exfoliated	–0.0162 (G)	–	83–373	488	Calizo et al. [22]
2L graphene	Supported, exfoliated	–0.0154 (G)	–	113–373	488	Calizo et al. [22]

[26, 41], few-layer and bulk MoS_2 [32, 41]. The larger phonon frequency shift of the out of plane $A_{1g}(\Gamma)$ mode in 1L has been attributed to stronger coupling between $A_{1g}(\Gamma)$ phonons and electrons than the electron–$E^1_{2g}(\Gamma)$ phonon coupling [41].

Furthermore, the thermal conductivities of suspended 1L- and 2L-WS_2 were investigated. In order to obtain the intrinsic thermal conductivities of WS_2 layers, it is necessary to exploit suspended samples because the substrate may influence the heat dissipation due to the phonon leakage in the vicinity of interfaces between the material and the substrate as observed for supported graphene samples [25, 46]. Micro-Raman spectroscopy has previously been used to study the thermal conductivities of 2D materials [24, 26]. The hole and the laser beam sizes are important parameters to determine the accurate thermal conductivity. In our case, the hole size is ~6 μm in diameter (Fig. 5(a)), which is much larger than the laser spot size (~0.5 μm). The laser-induced heat flows radially from the centre of the suspended WS_2 layers towards the edge of the hole, as evidenced by the theoretical simulation. Raman spectra for the $A_{1g}(\Gamma)$ peaks of 1L- and 2L-WS_2 at various laser powers are shown in Figs. 6(a) and 6(b), respectively. As the laser power increases, the $A_{1g}(\Gamma)$ peak intensity increases and its frequency red-shifts. The power dependences of the $A_{1g}(\Gamma)$ peak positions for 1L- and 2L-WS_2 are shown in Figs. 6(c) and 6(d), respectively. The linear red-shifts of the $A_{1g}(\Gamma)$ peaks in both 1L- and 2L samples reflect the local temperature rise in suspended layers. The slopes of $\Delta\omega/\Delta P$ are –7.85 ± 0.3 and –3.74 ± 0.2 cm^{-1}/mW for 1L- and 2L-WS_2, respectively.

It should be noted that the $E^1_{2g}(\Gamma)$ mode also shows a red-shift behaviour with increasing laser power (the data are not shown here) but its peak overlaps with other Raman peaks, and thus, the $A_{1g}(\Gamma)$ peak was selected for determining the thermal conductivity of the WS_2 flake.

The thermal conductivity can be evaluated by use of the experimental data from temperature- and power-dependent Raman measurements together with a recently developed heat diffusion model for 2D materials of graphene [25] and 1L MoS_2 [26]. The heat diffusion in the suspended region can be expressed as

$$\kappa\frac{1}{r}\frac{\mathrm{d}}{\mathrm{d}r}\left[r\frac{\mathrm{d}T_{\mathrm{i}}(r)}{\mathrm{d}r}\right]+q(r)=0 \quad \text{for } r<0 \tag{2}$$

where κ is the thermal conductivity of suspended WS_2 layers, $T_i(r)$ is the temperature distribution inside the hole, r is the position measured from the centre of the hole and R = 3 μm is the radius of hole. The $q(r)$ in Eq. (2) represents the volumetric optical heating, where the absorbed excitation power at 532 nm (~4%

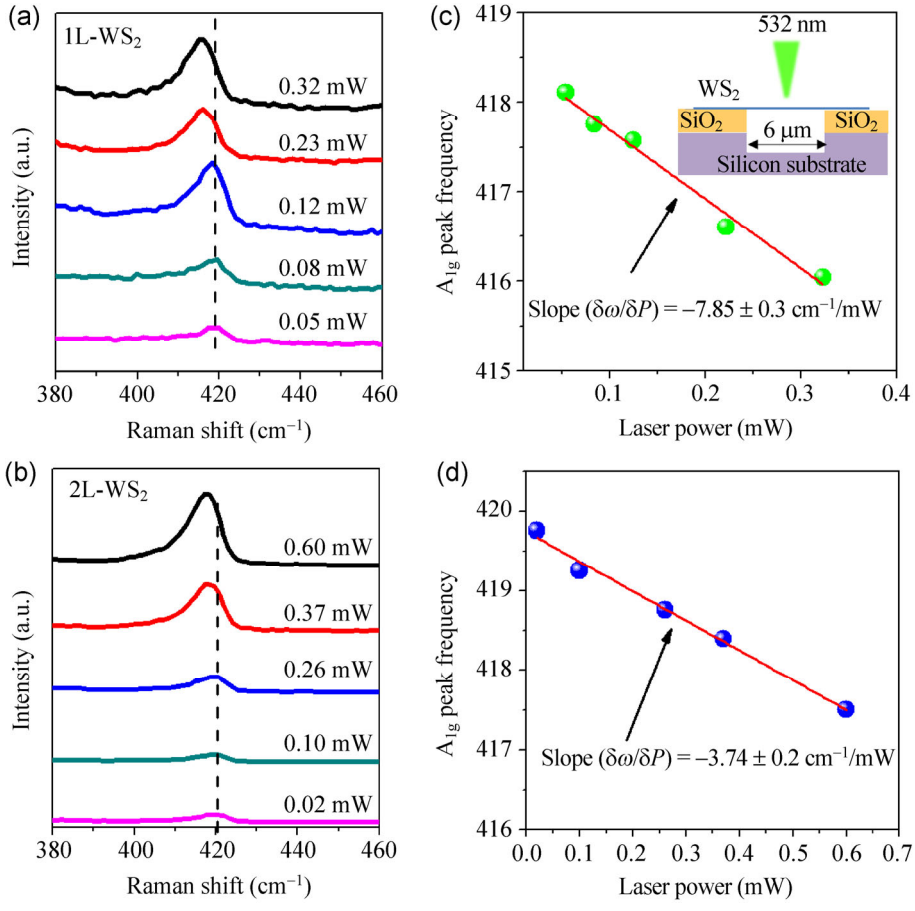

Figure 6 Raman spectra of suspended (a) 1L- and (b) 2L-WS_2, recorded at different excitation laser power. Power dependence of the $A_{1g}(\Gamma)$ peak frequencies (spheres) for suspended (c) 1L- and (d) 2L-WS_2, including linear fits of experimental data. The inset in (c) is a cross-section schematic of the thermal conductivity measurement, illustrating the suspended WS_2 layers and the size of the excitation laser beam compared with the diameter of a hole.

per layer) is used [15] (see the ESM for details). Note that, no additional metallic heat sink layers [25] (e.g. Au film) are used in our case, since metals may significantly modify the properties of 1L TMD [47]. Instead of using an additional heat sink, the heat transfer outside the suspended region and the boundary conditions have been considered in order to calculate the temperature profile, following to the method used in a recent study [26]. More details are given in the ESM. Figures 7(a) and 7(b) show the temperature profiles across the hole of 1L- and 2L-WS_2, respectively, simulated under various laser powers used in the measurements. The focused laser spot at the centre of the suspended region results in a rise of local temperature and the heat dissipates from the centre towards the edge of the hole due to the temperature difference. In the area near the boundary of the hole, the temperature nearly reaches the ambient temperature of 300 K. The spatial distributions of temperature over the suspended 1L and 2L WS_2 at the maximum laser powers used were calculated, as shown in Figs. 7(c) and 7(d), respectively. Temperature changes caused by the excitation beam mostly occur within the suspended areas with the diameter of 6 μm.

To build a relationship between the Raman data and the temperature calculations, the average temperature (inside the laser spot) induced by the laser excitation in our Raman measurements has been formulated as [25, 26]

$$T_m \approx \frac{\int_0^R T_i(r)q(r)\mathrm{d}r}{\int_0^R q(r)r\mathrm{d}r} \quad (3)$$

where $T_i(r)$ is related to the thermal conductivity of κ

as described in Eq. (2). Furthermore, the dependences of $\delta T_m/\delta P$ on the thermal conductivities of 1L and 2L WS_2 have been calculated, as shown in Figs. 7(e) and 7(f), respectively. The experimental values of $\delta T_m/\delta P$ for 1L- and 2L-WS_2 are 5.45×10^5 and 3.28×10^5 K/W, respectively, as determined by using the slopes from both temperature- and power-dependent Raman shifts of the A_{1g} modes. By use of these experimental values of $\delta T_m/\delta P$ and the theoretical relationships (the solid curves in Figs. 7(e) and 7(f)) between $\delta T_m/\delta P$ and κ for 1L- and 2L-WS_2, values of the thermal conductivity of 32 and 53 W/(m·K) are extracted for 1L- and 2L-WS_2, respectively.

Previous studies have shown that the thermal conductivities for suspended layered samples may be affected by the fabrication process, the method of determination, the sample size (i.e. thickness and area), and environmental contamination [25, 48, 49]. For instance, the reported thermal conductivities for suspended graphene samples at room temperature vary over a broad range from 1,500–5,000 W/(m·K) [25, 48, 49]. To acquire an intuitive understanding of the values we obtained for κ in 1L- and 2L-WS_2, Table 2 summarizes thermal conductivities of 2D materials, including suspended WS_2, MoS_2, h-BN and graphene flakes. The thermal conductivities of 1L- and 2L-WS_2

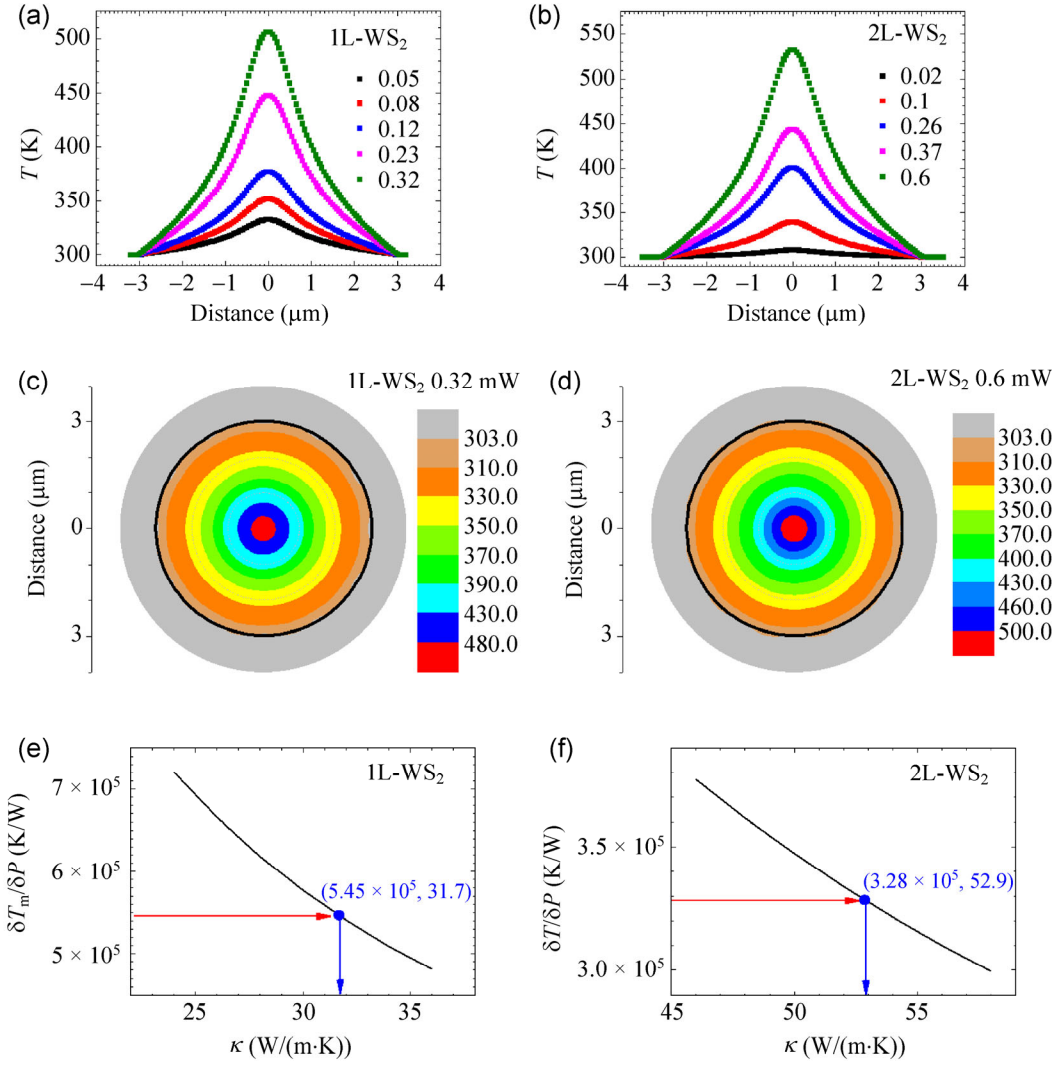

Figure 7 Calculated temperature profiles for (a) 1L- and (b) 2L-WS_2 at various excitation powers (units of mW). Simulated spatial temperature distributions for (c) 1L- and (d) 2L-WS_2 at the excitation powers of 0.32 and 0.6 mW. Plots of $\delta T/\delta P$ versus κ for (e) 1L- and (f) 2L-WS_2. Solid curves are the theoretical predicted relationships. Blue dots are the positions corresponding to experimental observations.

Table 2 Thermal conductivities of 2D materials at around room temperature

Sample type	Comment	κ (W/(m·K))	Methods	Ref.
1L-suspended WS_2	CVD (transferred)	32	Raman	This work
2L-suspended WS_2	CVD (transferred)	53	Raman	This work
1L-suspended MoS_2	Pristine (exfoliated)	34	Raman	Yan et al. [26]
Few layer-suspended MoS_2	CVD (transferred)	52	Raman	Sahoo et al. [32]
5- and 11-layer h-BN	Pristine (transferred)	250, 360	Microbridge	Jo et al. [23]
1L-suspended graphene	Pristine (exfoliated)	~4,840–5,300	Raman	Baladin et al. [24]
1L-suspended graphene	CVD (transferred)	~1,450–3,600	Raman	Cai et al. [25]
2L-suspended graphene	CVD (transferred)	~560–620	Thermometer	Pettes et al. [48]

are comparable with those of exfoliated 1L-MoS_2 (34 W/(m·K)) and few layer MoS_2 (52 W/(m·K)) grown by a vapor-phase method [26, 32], and are one/two orders smaller than that of BN/graphene [23, 24]. A knowledge about the thermal conduction properties of 1L- and 2L-WS_2 will significantly promote their applications in semiconducting devices. As an alternative to conducting graphene, the recent developments in 2D semiconductors (e.g. TMD monolayers) could play a revolutionary role in the future development of electronics and optoelectronics.

3 Conclusions

We report the temperature and excitation dependences of the first-order $E^1_{2g}(\Gamma)$ and $A_{1g}(\Gamma)$ Raman modes of CVD-grown 1L- and 2L-WS_2. It was found that $E^1_{2g}(\Gamma)$ and $A_{1g}(\Gamma)$ peak frequencies decrease with increasing temperature for both supported and suspended samples. The temperature coefficient of the $A_{1g}(\Gamma)$ mode is larger than that of the mode in 1L-WS_2. This is due to stronger electron–A_{1g} phonon coupling in 1L-WS_2 than that of the $E^1_{2g}(\Gamma)$ mode. Employing the local heating effect of the laser power on the suspended samples, the thermal conductivities at room temperature were estimated to be 32 W/(m·K) for 1L-WS_2 and 53 W/(m·K) for 2L-WS_2. Our experimental results provide an understanding of the heat dissipation and fundamental thermal parameters in atomically thin WS_2 layers, which should make a significant contribution to the development of device applications based on 2D semiconductors.

4 Experimental

1L- and 2L-WS_2 samples were grown by CVD on SiO_2/Si substrates [13, 15]. For the suspended samples, the as-grown WS_2 layers were transferred onto the substrates with holes of 3–6 μm in diameter prepared by the reactive ion etching technique. The depth of the hole on the substrate is ~3 μm. The transfer procedure was carried out according to previous work [50]. The thicknesses of the samples were measured by AFM and confirmed by PL and Raman spectrometers. Micro-Raman and PL measurements were carried out using a WITEC Raman system with 488 and 532 nm excitation lasers. The laser spot size was determined by the line-scan profile of the Raman signal across the sharp sample edge. In the temperature-dependent Raman measurements, a 50× objective lens with a long working distance and a numerical aperture (NA) of 0.55 was used. The laser beam size was ~1 μm. The temperature was controlled by a thermal stage (Linkam) in a vacuum chamber cooled by the liquid nitrogen. To avoid heating induced by the excitation laser, the laser power was maintained at ~40 μW throughout all the measurements. In the power- dependent measurements, a 100× objective lens with NA = 0.95 was used. The laser beam spot was approximately 0.5 μm. The Raman spectra were taken from suspended 1L and 2L samples, in which the samples were excited by different laser powers varying from 0.02 to 0.6 mW, which are known not to damage the WS_2 layers [32].

Acknowledgements

This work is supported by the Singapore National Research Foundation under NRF RF award (No. NRF-RF2010-07), MOE Tier 2 (No. MOE2012-T2-2-049) and A*Star SERC PSF grant (No. 1321202101).

Electronic Supplementary Material: Supplementary material (optical image, fluorescence images and PL of MoS_2, Raman spectra of 1L-WS_2 taken at 140 and 380 K and the peak frequencies of the E^1_{2g} and A_{1g} modes for suspended and supported 1L- and 2L-WS_2) is available in the online version of this article at http://dx.doi.org/10.1007/s12274-014-0602-0.

References

[1] Wang, Q. H.; Kalantar-Zadeh, K.; Kis, A.; Coleman, J. N.; Strano, M. S. Electronics and optoelectronics of two-dimensional transition metal dichalcogenides. *Nat. Nanotechnol.* **2012**, *7*, 699–712.

[2] Novoselov, K. S. Nobel lecture: Graphene: Materials in the flatland. *Rev. Mod. Phys.* **2011**, *83*, 837–849.

[3] Neto, A. H. C.; Novoselov, K. New directions in science and technology: Two-dimensional crystals. *Rep. Prog. Phys.* **2011**, *74*, 082521.

[4] Mak, K. F.; Lee, C.; Hone, J.; Shan, J.; Heinz, T. F. Atomically thin Mos_2: A new direct-gap semiconductor. *Phys. Rev. Lett.* **2010**, *105*, 136805.

[5] Splendiani, A.; Sun, L.; Zhang, Y. B.; Li, T. S.; Kim, J.; Chim, C. Y.; Galli, G.; Wang, F. Emerging photoluminescence in monolayer MoS_2. *Nano Lett.* **2010**, *10*, 1271–1275.

[6] Tonndorf, P.; Schmidt, R.; Böttger, P.; Zhang, X.; Börner, J.; Liebig, A.; Albrecht, M.; Kloc, C.; Gordan, O.; Zahn, D. R. T. et al. Photoluminescence emission and Raman response of monolayer MoS_2, $MoSe_2$, and WSe_2. *Opt. Exp.* **2013**, *21*, 4908–4916.

[7] Zhao, W. J.; Ghorannevis, Z.; Chu, L. Q.; Toh, M.; Kloc, C.; Tan, P. H.; Eda, G. Evolution of Electronic Structure in Atomically Thin Sheets of WS_2 and WSe_2. *ACS Nano* **2013**, *7*, 791–797.

[8] Radisavljevic, B.; Radenovic, A.; Brivio, J.; Giacometti, V.; Kis, A. Single-layer MoS_2 transistors. *Nat. Nanotechnol.* **2011**, *6*, 147–150.

[9] Kuc, A.; Zibouche, N.; Heine, T. Influence of quantum confinement on the electronic structure of the transition metal sulfide TS_2. *Phys. Rev. B* **2011**, *83*, 245213.

[10] Zeng, H. L.; Liu, G. B.; Dai, J. F.; Yan, Y. J.; Zhu, B. R.; He, R. C.; Xie, L.; Xu, S. J.; Chen, X. H.; Yao, W. et al. Optical signature of symmetry variations and spin-valley coupling in atomically thin tungsten dichalcogenides. *Sci. Rep.* **2013**, *3*, 1608.

[11] Voiry, D.; Yamaguchi, H.; Li, J. W.; Silva, R.; Alves, D. C. B.; Fujita, T.; Chen, M. W.; Asefa, T.; Shenoy, V. B.; Eda, G. et al. Enhanced catalytic activity in strained chemically exfoliated WS_2 nanosheets for hydrogen evolution. *Nat. Mater.* **2013**, *12*, 850–855.

[12] Gutiérrez, H. R.; Perea-López, N.; Elías, A. L.; Berkdemir, A.; Wang, B.; Lv, R.; López-Urías, F.; Crespi, V. H.; Terrones, H.; Terrones, M. Extraordinary room-temperature photoluminescence in triangular WS_2 monolayers. *Nano Lett.* **2013**, *13*, 3447–3454.

[13] Cong, C. X.; Shang, J. Z.; Wu, X.; Cao, B. C.; Peimyoo, N.; Qiu, C. Y.; Sun, L. T.; Yu, T. Synthesis and optical properties of large-area single-crystalline 2D semiconductor WS_2 monolayer from chemical vapor deposition. *Adv. Opt. Mater.* **2014**, *2*, 131–136.

[14] Zhang, Y.; Zhang, Y. F.; Ji, Q. Q.; Ju, J.; Yuan, H. T.; Shi, J. P.; Gao, T.; Ma, D. L.; Liu, M. X.; Chen, Y. B. et al. Controlled growth of high-quality monolayer WS_2 layers on sapphire and imaging its grain boundary. *ACS Nano* **2013**, *7*, 8963–8971.

[15] Peimyoo, N.; Shang, J. Z.; Cong, C. X.; Shen, X. N.; Wu, X. Y.; Yeow, E. K. L.; Yu, T. Nonblinking, intense two-dimensional light emitter: Mono layer WS_2 triangles. *ACS Nano* **2013**, *7*, 10985–10994.

[16] Song, J. G.; Park, J.; Lee, W.; Choi, T.; Jung, H.; Lee, C. W.; Hwang, S. H.; Myoung, J. M.; Jung, J. H.; Kim, S. H. et al. Layer-controlled, wafer-scale, and conformal synthesis of tungsten disulfide nanosheets using atomic layer deposition. *ACS Nano* **2013**, *7*, 11333–11340.

[17] Braga, D.; Lezama, I. G.; Berger, H.; Morpurgo, A. F. Quantitative determination of the band gap of WS_2 with ambipolar ionic liquid-gated transistors. *Nano Lett.* **2012**, *12*, 5218–5223.

[18] Mak, K. F.; He, K. L.; Shan, J.; Heinz, T. F. Control of valley polarization in monolayer MoS_2 by optical helicity. *Nat. Nanotechnol.* **2012**, *7*, 494–498.

[19] Zeng, H. L.; Dai, J. F.; Yao, W.; Xiao, D.; Cui, X. D. Valley polarization in MoS_2 monolayers by optical pumping. *Nat. Nanotechnol.* **2012**, *7*, 490–493.

[20] Cao, T.; Wang, G.; Han, W. P.; Ye, H. Q.; Zhu, C. R.; Shi, J. R.; Niu, Q.; Tan, P. H.; Wang, E.; Liu, B. L. et al. Valley-selective circular dichroism of monolayer molybdenum disulphide. *Nat. Commun.* **2012**, *3*, 887.

[21] Cong, C. X.; Yu, T. Enhanced ultra-low-frequency interlayer shear modes in folded graphene layers. *Nat. Commun.* **2014**, *5*, 4709.

[22] Calizo, I.; Balandin, A. A.; Bao, W.; Miao, F.; Lau, C. N. Temperature dependence of the Raman spectra of graphene and graphene multilayers. *Nano Lett.* **2007**, *7*, 2645–2649.

[23] Jo, I.; Pettes, M. T.; Kim, J.; Watanabe, K.; Taniguchi, T.; Yao, Z.; Shi, L. Thermal conductivity and phonon transport in suspended few-layer hexagonal boron nitride. *Nano Lett.* **2013**, *13*, 550–554.

[24] Balandin, A. A.; Ghosh, S.; Bao, W. Z.; Calizo, I.; Teweldebrhan, D.; Miao, F.; Lau, C. N. Superior thermal conductivity of single-layer graphene. *Nano Lett.* **2008**, *8*, 902–907.

[25] Cai, W. W.; Moore, A. L.; Zhu, Y. W.; Li, X. S.; Chen, S. S.; Shi, L.; Ruoff, R. S. Thermal transport in suspended and supported monolayer graphene grown by chemical vapor deposition. *Nano Lett.* **2010**, *10*, 1645–1651.

[26] Yan, R. S.; Simpson, J. R.; Bertolazzi, S.; Brivio, J.; Watson, M.; Wu, X. F.; Kis, A.; Luo, T. F.; Walker, A. R. H.; Xing, H. G. Thermal conductivity of monolayer molybdenum disulfide obtained from temperature-dependent Raman spectroscopy. *ACS Nano* **2014**, *8*, 986–993.

[27] Li, H.; Zhang, Q.; Yap, C. C. R.; Tay, B. K.; Edwin, T. H. T.; Olivier, A.; Baillargeat, D. From bulk to monolayer MoS_2: Evolution of Raman scattering. *Adv. Funct. Mater.* **2012**, *22*, 1385–1390.

[28] Hajiyev, P.; Cong, C. X.; Qiu, C. Y.; Yu, T. Contrast and Raman spectroscopy study of single- and few-layered charge density wave material: 2H-$TaSe_2$. *Sci. Rep.* **2013**, *3*, 2593.

[29] Chakraborty, B.; Bera, A.; Muthu, D. V. S.; Bhowmick, S.; Waghmare, U. V.; Sood, A. K. Symmetry-dependent phonon renormalization in monolayer MoS_2 transistor. *Phys. Rev. B* **2012**, *85*, 161403.

[30] Peimyoo, N.; Li, J. W.; Shang, J. Z.; Shen, X. N.; Qiu, C. Y.; Xie, L. H.; Huang, W.; Yu, T. Photocontrolled molecular structural transition and doping in graphene. *ACS Nano* **2012**, *6*, 8878–8886.

[31] Wang, Y. L.; Cong, C. X.; Qiu, C. Y.; Yu, T. Raman spectroscopy study of lattice vibration and crystallographic orientation of monolayer MoS_2 under uniaxial strain. *Small* **2013**, *9*, 2857–2861.

[32] Sahoo, S.; Gaur, A. P. S.; Ahmadi, M.; Guinel, M. J. F.; Katiyar, R. S. Temperature-dependent Raman studies and thermal conductivity of few-layer MoS_2. *J. Phys. Chem. C* **2013**, *117*, 9042–9047.

[33] Thripuranthaka, M.; Late, D. J. Temperature dependent phonon shifts in single-layer WS_2. *ACS Appl. Mater. Inter.* **2014**, *6*, 1158–1163.

[34] Kam, K. K.; Parkinson, B. A. Detailed photocurrent spectroscopy of the semiconducting group-VI transition-metal dichalcogenides. *J. Phys. Chem.* **1982**, *86*, 463–467.

[35] Sourisseau, C.; Cruege, F.; Fouassier, M.; Alba, M. Second-order Raman effects, inelastic neutron scattering and lattice dynamics in 2H-WS_2. *Chem. Phys.* **1991**, *150*, 281–293.

[36] Sekine, T.; Nakashizu, T.; Toyoda, K.; Uchinokura, K.; Matsuura, E. Raman scattering in layered compound 2H-WS_2. *Solid State Commun.* **1980**, *35*, 371–373.

[37] Berkdemir, A.; Gutiérrez, H. R.; Botello-Méndez, A. R.; Perea-López, N.; Elías, A. L.; Chia, C. I.; Wang, B.; Crespi, V. H.; López-Urías, F.; Charlier, J. C. et al. Identification of individual and few layers of WS_2 using Raman spectroscopy. *Sci. Rep.* **2013**, *3*, 1755.

[38] Zhang, X.; Han, W. P.; Wu, J. B.; Milana, S.; Lu, Y.; Li, Q. Q.; Ferrari, A. C.; Tan, P. H. Raman spectroscopy of shear and layer breathing modes in multilayer MoS_2. *Phys. Rev. B* **2013**, *87*, 115413.

[39] Molina-Sánchez, A.; Wirtz, L. Phonons in single-layer and few-layer MoS_2 and WS_2. *Phys. Rev. B* **2011**, *84*, 155413.

[40] Lee, C.; Yan, H. G.; Brus, L. E.; Heinz, T. F.; Hone, J.; Ryu, S. Anomalous lattice vibrations of single- and few-layer MoS_2. *ACS Nano* **2010**, *4*, 2695–2700.

[41] Lanzillo, N. A.; Birdwell, A. G.; Amani, M.; Crowne, F. J.; Shah, P. B.; Najmaei, S.; Liu, Z.; Ajayan, P. M.; Lou, J.; Dubey, M. et al. Temperature-dependent phonon shifts in monolayer MoS_2. *Appl. Phys. Lett.* **2013**, *103*, 93102.

[42] Peercy, P. S.; Morosin, B. Pressure and temperature dependences of Raman-active phonons in SnO_2. *Phys. Rev. B* **1973**, *7*, 2779–2786.

[43] Tan, P. H.; Deng, Y. M.; Zhao, Q.; Cheng, W. C. The intrinsic temperature effect of the Raman spectra of graphite. *Appl. Phys. Lett.* **1999**, *74*, 1818–1820.

[44] Horzum, S.; Sahin, H.; Cahangirov, S.; Cudazzo, P.; Rubio, A.; Serin, T.; Peeters, F. M. Phonon softening and direct to indirect band gap crossover in strained single-layer $MoSe_2$. *Phys. Rev. B* **2013**, *87*, 125415.

[45] Scheuschner, N.; Ochedowski, O.; Kaulitz, A. M.; Gillen, R.; Schleberger, M.; Maultzsch, J. Photoluminescence of freestanding single- and few-layer MoS_2. *Phys. Rev. B* **2014**, *89*, 125406.

[46] Seol, J. H.; Jo, I.; Moore, A. L.; Lindsay, L.; Aitken, Z. H.; Pettes, M. T.; Li, X. S.; Yao, Z.; Huang, R.; Broido, D. et al. Two-dimensional phonon transport in supported graphene. *Science* **2010**, *328*, 213–216.

[47] Gong, C.; Colombo, L.; Wallace, R. M.; Cho, K. The unusual mechanism of partial Fermi level pinning at metal–MoS_2 interfaces. *Nano Lett.* **2014**, *14*, 1714–1720.

[48] Pettes, M. T.; Jo, I.; Yao, Z.; Shi, L. Influence of polymeric residue on the thermal conductivity of suspended bilayer graphene. *Nano Lett.* **2011**, *11*, 1195–1200.

[49] Ghosh, S.; Bao, W. Z.; Nika, D. L.; Subrina, S.; Pokatilov, E. P.; Lau, C. N.; Balandin, A. A. Dimensional crossover of thermal transport in few-layer graphene. *Nat. Mater.* **2010**, *9*, 555–558.

[50] Van der Zande, A. M.; Huang, P. Y.; Chenet, D. A.; Berkelbach, T. C.; You, Y. M.; Lee, G. H.; Heinz, T. F.; Reichman, D. R.; Muller, D. A.; Hone, J. C. Grains and grain boundaries in highly crystalline monolayer molybdenum disulphide. *Nat. Mater.* **2013**, *12*, 554–561.